This article has been accepted for publication in a future issue of this journal, but has not been fully edited. Content may change prior to final publication. Citation information: DOI 10.1109/TIP.2018.2889914, IEEE Transactions on Image Processing

Weighted Tensor Rank-1 Decomposition for Nonlocal Image Denoising

Yue Wu, *Student Member, IEEE,* Leyuan Fang, *Senior Member, IEEE,* and Shutao Li, *Fellow, IEEE*

***Abstract*—Natural images often contain patches with high similarity. In this paper, to effectively utilize the local and nonlocal self-similarity for low-rank models, we propose a novel weighted tensor rank-1 decomposition method (terms as WTR1) for nonlocal image denoising. Although the low-rank approximation problem has been well studied for matrices, it remains elusive of the theoretically extension to tensors due to the NP-hard tensor decomposition. To tackle this problem, the proposed WTR1 method designs a new efficient CANDECOMP/PARAFAC (CP) decomposition algorithm and constructs a straightforward low-rank tensor approximation strategy. This is achieved by elegantly manipulating the CP-rank, called intrinsic low-rank tensor approximation. Specifically, the WTR1 method first groups similar patches into a 3-D stack and converts the stack into a finite sum of rank-1 products. Then, we deploy the intrinsic low-rank tensor approximation to produce the final denoised image. The proposed WTR1 method can jointly exploit the local and nonlocal self-similarity, thus improving the nonlocal image denoising quality. Experimental results have shown that the proposed WTR1 outperforms several state-of-the-art denoising methods.**

***Index Terms*—Image denoising, tensor decomposition, nonlocal similarity, low-rank approximation.**

I. Introduction

IMAGE denoising is a classical inverse problem in natural image processing, aiming to recover the original image from a noisy image. The basic denoising assumption is that the image has been contaminated with additive white Gaussian noise, and the variance of the noise is known. Mathematically, the noisy image $\mathbf{Y}$ can be decomposed into its original image $\mathbf{X}$ and zero-mean Gaussian distribution noise $\mathbf{N}$,

$$\mathbf{Y} = \mathbf{X} + \mathbf{N}. \tag{1}$$

To transform the image denoising task into a well-posed problem, many denoising models have been proposed by employing various natural image priors [1]-[9]. The classical total variation (TV) models assume that natural images satisfy a gradient minimization constraint [1]-[2], which is effective in removing the noise but tends to over-smooth the fine-detailed structures. By introducing a redundant representation [3]-[6], the sparse models assume that the clean image content can be effectively described by an over-complete dictionary, whereas the random noise mainly remains in the residuals. To learn the underlying image prior, deep learning is a flexible technique to achieve favorable denoising performance [7]-[9]. Compared with traditional denoising models, deep learning can automatically learn the model from training set of degraded and reference image pairs, which can avoid the complex optimization problem in the testing stage. However, deep learning requires a huge amount of noise-free training samples and also creates very heavy computational burden in the training process. In general, it is crucial to find an appropriate regulation of the true signal for denoising.

Recently, by operating patch grouping for sparsity enforcement and exploiting the global correlations hidden in data, the nonlocal self-similarity of natural images becomes an important driving force for enhancing the denoising performance [10]-[16]. A well-known example is the block-matching with 3-D filtering (BM3D) [11], which is always a denoising benchmark by utilizing nonlocal patch matching and collaborative filters. To reveal the intrinsic geometrical structures of natural images, the nuclear norm minimization (NNM) [19] assumes that nonlocal similar patches are low-rank and have sparse singular values. In [21], the NNM method has further been improved by regularizing the singular values with different weights. Note that, most of the existing nonlocal low-rank models are based on the degenerate matrix approach and treat each image patch as a vector. However, vector representation has ignored the local patch geometry which should be utilized for image denoising.

As an alternative, low-rank tensor approximation can be used to better describe the local and nonlocal structures of the grouped multidimensional data [22]-[24]. In [22], a tensor-based model using the higher order singular value decomposition (HOSVD) is proposed for natural image denoising. The HOSVD denoising method is a simple and effective technique by applying hard coefficient thresholding and Wiener filtering. However, the factorization-based truncation strategy adopted in the HOSVD cannot manipulate the tensor rank as that in matrices. To measure the sparsity of tensors, Liu *et al.* [25] heuristically introduced a tensor trace norm together with an unfolding approach. In view of the dependency among multiple constraints, they tackled the tensor problem with a combination of matrix convex program. In general, the multi-rank truncation applied in [25] is based on a matricization strategy, which is short of a natural physical interpretation. Zhao *et al.* [26] simply ameliorated the summation of tensor ranks by using the multiplication operation. To the best of our knowledge, the straightforward intrinsic low-rank tensor approximation has not been addressed in the open literature.

This work was supported by the National Natural Science Fund of China for International Cooperation and Exchanges under Grant 61520106001 and by the Fund of Hunan Province for Science and Technology Plan Project under Grant 2017RS3024.

Y. Wu, L. Fang, and S. Li are with the College of Electrical and Information Engineering, Hunan University, Changsha 410082, China, and also with the Key Laboratory of Visual Perception and Artificial Intelligence of Hunan Province, Changsha, 410082, China (e-mail: yuewu@hnu.edu.cn; fangleyuan@gmail.com; shutao_li@hnu.edu.cn).

1057-7149 (c) 2018 IEEE. Personal use is permitted, but republication/redistribution requires IEEE permission. See http://www.ieee.org/publications_standards/publications/rights/index.html for more information.

This article has been accepted for publication in a future issue of this journal, but has not been fully edited. Content may change prior to final publication. Citation information: DOI 10.1109/TIP.2018.2889914, IEEE Transactions on Image Processing

The major challenge lies in a feasible tensor decomposition algorithm like matrices.

To address the above problems, this paper proposes a novel weighted tensor rank-1 decomposition method (terms as WTR1) for nonlocal image denoising. The proposed WTR1 method provides a feasible and effective strategy for intrinsic low-rank tensor approximation and improves the recovery with a weighting approach. In specific, by developing a new efficient CP decomposition algorithm, the proposed WTR1 method can elegantly manipulate the CP-rank, which is naturally a straightforward low-rank extension of matrix case. In comparison with the classical CP-alternating least squares (CP-ALS) method [27], [38], the proposed decomposition algorithm can conveniently convert a tensor into a finite sum of rank-1 outer products, and we do not need to pre-define the tensor rank. Specifically, for a testing noisy image, we first search similar patches for each exemplar patch and transfer these similar patches into a 3-D stack. Then, the 3-D stack is converted into a finite sum of rank-1 products to deploy the intrinsic low-rank tensor approximation. Finally, the estimated patches are accumulated in image space, and each pixel is averaged to obtain the final denoised image.

The rest of the paper is organized as follows. Sections II and III briefly review preliminaries and related works. The proposed WTR1 method for nonlocal image denoising is described in Section IV. Experimental results and comparisons with several state-of-the-art algorithms are shown in Section V. Finally, we conclude and suggest some future works in Section VI.

II. Notations and Preliminaries

In this paper, light italic letters denote scalars (e.g., A and a), bold lower-case letters represent vectors (e.g., $\mathbf{a}$), bold upper-case letters stand for matrices (e.g., $\mathbf{A}$), and bold calligraphic letters denote tensors (e.g., $\boldsymbol{\mathcal{A}}$). Indices typically range from 1 to their capital version, e.g., $i = 1, 2, \ldots, I$. An arbitrary Nth-order tensor, corresponding to an N dimensional array, is represented as $\boldsymbol{\mathcal{X}} \in \mathbb{R}^{I_1 \times I_2 \times \cdots \times I_N}$, where $I_1, I_2, \ldots, I_N$ are the sizes of tensor dimensions, respectively. The number of tensor dimensions is known as orders, ways or modes.

Definition 1 (The Product of a Tensor with a Matrix): The n-mode product of a tensor $\boldsymbol{\mathcal{X}} \in \mathbb{R}^{I_1 \times I_2 \times \cdots \times I_N}$ with a matrix $\mathbf{U} \in \mathbb{R}^{J \times I_n}$ is defined as

$$(\boldsymbol{\mathcal{X}} \times_n \mathbf{U})_{i_1 \ldots i_{n-1} j i_{n+1} \ldots i_N} = \sum_{i_n=1}^{I_n} x_{i_1 i_2 \ldots i_N} u_{j i_n}, \quad (2)$$

where x and u are scalars corresponding to $\boldsymbol{\mathcal{X}}$ and $\mathbf{U}$, respectively, and so $\boldsymbol{\mathcal{X}} \times_n \mathbf{U} \in \mathbb{R}^{I_1 \times \cdots \times I_{n-1} \times J \times I_{n+1} \times \cdots \times I_N}$.

Definition 2 (Rank-1 Tensor): An Nth-order tensor $\boldsymbol{\mathcal{X}}$ is rank-1 if it can be written as the outer product of N vectors, i.e.,

$$\boldsymbol{\mathcal{X}} = \mathbf{a}^{(1)} \circ \mathbf{a}^{(2)} \circ \cdots \circ \mathbf{a}^{(N)}, \quad (3)$$

where $\circ$ denotes the vector outer product, and $\mathbf{a}$ is a factor vector.

Definition 3 (CP-Rank): The CP-rank of an Nth-order tensor $\boldsymbol{\mathcal{X}}$ is defined as

$$\text{rank}_{\text{CP}}(\boldsymbol{\mathcal{X}}) = \min\{R \mid \boldsymbol{\mathcal{X}} = \sum_{r=1}^{R} \mathbf{a}_r^{(1)} \circ \mathbf{a}_r^{(2)} \circ \cdots \circ \mathbf{a}_r^{(N)}\}, \quad (4)$$

where R is the CP-rank of $\boldsymbol{\mathcal{X}}$. In other words, the CP-rank is defined as the minimum number of components in the decomposition.

III. Related Works

A. Problem Formulation

As described in [28]-[30], some explicit or implicit assumptions are critical to the solution of image denoising. By selecting an appropriate regularization parameter ρ to balance the relative contribution between likelihood term and prior term, the problem (1) can be generally formulated as

$$\hat{\mathbf{X}} = \arg\min_{\mathbf{X}} \|\mathbf{Y} - \mathbf{X}\|_F^2 + \rho \cdot \Psi(\mathbf{X}), \quad (5)$$

where $\|\mathbf{Y} - \mathbf{X}\|_F^2$ indicates the conformity between the true image $\mathbf{X}$ and the observation $\mathbf{Y}$, and $\Psi(\mathbf{X})$ is a function to regularize certain priors.

B. Low-Rank Tensor Approximation

In the matrix-based works, the low-rank matrix factorization (LRMF) [31]-[34] and the nuclear norm minimization (NNM) [18]-[21] are generally imposed on the low-rank approximation. The LRMF aims to find two low-rank matrices whose product is close to a given matrix, and this is basically a nonconvex optimization problem. The NNM is defined as the sum of its singular values. One distinct advantage of the NNM lies in that it is the tightest convex approximation for the matrix rank [35].

Particularly, the low-rank tensor approximation problem is the generalization of the matrix concept. Compared with the natural sparsity measure (rank) for matrices, tensor representation is a more appropriate technique to describe the intrinsic correlations along various tensor modes. The Tucker decomposition [36] is a typical model to express a tensor into the product of a core tensor and several factor matrices along each mode. An efficient realization is computed by the HOSVD [37]. Given an Nth-order tensor $\boldsymbol{\mathcal{X}}$, the HOSVD is given as follows:

$$\begin{aligned} \boldsymbol{\mathcal{X}} &= \sum_{r_1}^{R_1} \sum_{r_2}^{R_2} \cdots \sum_{r_N}^{R_N} \mathcal{G}_{r_1 r_2 \ldots r_N} \circ \mathbf{u}_{r_1}^{(1)} \circ \mathbf{u}_{r_2}^{(2)} \circ \cdots \circ \mathbf{u}_{r_N}^{(N)} \\ &= \mathcal{G} \times_1 \mathbf{U}^{(1)} \times_2 \mathbf{U}^{(2)} \cdots \times_N \mathbf{U}^{(N)}, \end{aligned} \quad (6)$$

where $\mathcal{G}$ is an Nth-order core tensor, and $\mathbf{U}$ is a factor matrix. Note that, the Tucker decomposition cannot be used to regularize the tensor rank since it is not necessarily canonical. To generalize the low-rank matrix case to higher order tensors, Liu *et al.* [25] introduced a definition of the tensor trace norm which is processed by combining the nuclear norms of all

1057-7149 (c) 2018 IEEE. Personal use is permitted, but republication/redistribution requires IEEE permission. See http://www.ieee.org/publications_standards/publications/rights/index.html for more information.

This article has been accepted for publication in a future issue of this journal, but has not been fully edited. Content may change prior to final publication. Citation information: DOI 10.1109/TIP.2018.2889914, IEEE Transactions on Image Processing

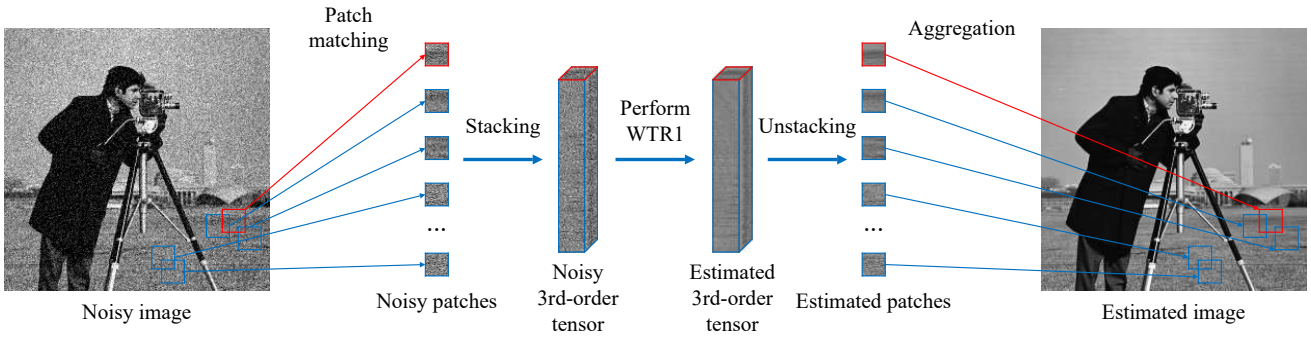

Fig. 1. Flowchart of the proposed WTR1 denoising method.

matrices unfolded along each mode, and the matricization-based tensor trace norm can be expressed as the following convex program:

$$\min_{\mathcal{X}\in\mathbb{R}^{I_1\times I_2\times\cdots\times I_N}} \sum_{n=1}^{N} \alpha_n \|\mathbf{X}_{(n)}\|_*, \tag{7}$$

where $\mathbf{X}_{(n)} \in \mathbb{R}^{I_n\times(\prod_{k\neq n} I_k)}$ is the unfolded tensor whose columns are the mode-n fibers of $\mathcal{X}$, $\|\cdot\|_*$ denotes the nuclear norm, α_n is a constant satisfying $\alpha_n \geq 0$ and $\sum_{n=1}^{N} \alpha_n = 1$. Such separated matricization operation lacks a clear physical meaning and a consistent relationship with sparsity measures for matrices. To address this issue, the faithful intrinsic low-rank tensor approximation based on the CP-rank regularization is a more innocent and satisfactory task. The CP decomposition is to factorize a tensor as the sum of a finite number of rank-1 tensors, and it is expected to be written as

$$\mathcal{X} = \sum_{r=1}^{R} \mathbf{a}_r^{(1)} \circ \mathbf{a}_r^{(2)} \circ \cdots \circ \mathbf{a}_r^{(N)}, \tag{8}$$

where R is the CP-rank of $\mathcal{X}$. However, the task of rank R computing is an NP-hard problem, and we can only give the weak upper bound of the CP-rank [38]. Usually, CP low-rank tensor approximation models are performed by first setting the number K of rank-1 components, and $\mathcal{X}$ is approximated by minimizing

$$\min_{\hat{\mathcal{X}}} \|\mathcal{X} - \hat{\mathcal{X}}\|_T^2 + \rho \cdot \|\mathcal{X} - \sum_{r=1}^{K} \mathbf{a}_r^{(1)} \circ \mathbf{a}_r^{(2)} \circ \cdots \circ \mathbf{a}_r^{(N)}\|_T^2, \tag{9}$$

where the Frobenius norm of a tensor $\mathcal{X}$ is defined as: $\|\mathcal{X}\|_T = (\sum_{i_1,i_2,\ldots,i_N} |\mathbf{x}_{i_1 i_2 \ldots i_N}|^2)^{1/2}$.

In general, tensor recovery remains to be a complicated problem because of the difficulty in the decomposition.

IV. Proposed WTR1 Denoising Method

In this Section, we propose the WTR1 method for nonlocal image denoising, which can effectively utilize the local and nonlocal self-similarity jointly for low-rank models. To extend the low-rank matrix case to tensors, we develop the intrinsic low-rank tensor approximation by manipulating the CP-rank. Concretely, to effectively utilize the information in the grouped similar patches, the proposed WTR1 method represents each patch in the form of matrix and groups them into a 3-D stack. Then, we convert the stack into a finite sum of rank-1 tensors and obtain a set of associated singular values to efficiently regularize the CP-rank. The whole denoising procedure is illustrated in Fig. 1. More details of the proposed WTR1 method are demonstrated in the following subsections.

A. Modeling of WTR1 for Nonlocal Image Denoising

The proposed WTR1 method mainly consists of two steps: patch grouping and low-rank approximation. Firstly, for each exemplar patch $\mathbf{X}_i$, we search for similar patches within a local window. The legitimacy is from the assumption that similar patches often can be found in the local region. The grouped 3-D stack is composed by multiple 2-D similar patches, which can be naturally regarded as a third-order tensor. Specifically, the similar patches are identified by the Euclidean distance-based similarity metric. Secondly, we employ the intrinsic low-rank tensor approximation achieved by regularizing the CP-rank. With a weighting term, we formulate the following optimization model for nonlocal image denoising:

$$\begin{aligned}\min_{\mathbf{X},\lambda_{i,r},\mathbf{u}_{i,r}^{(1)},\mathbf{u}_{i,r}^{(2)},\mathbf{u}_{i,r}^{(3)}} & \|\mathbf{Y}-\mathbf{X}\|_F^2 \\ & + \rho \sum_i \|\tilde{\mathcal{R}}_i\mathbf{X} - \sum_r \omega_{i,r}\lambda_{i,r}\mathbf{u}_{i,r}^{(1)} \circ \mathbf{u}_{i,r}^{(2)} \circ \mathbf{u}_{i,r}^{(3)}\|_T^2,\end{aligned} \tag{10}$$

where $\lambda_{i,r}$ is the singular value affiliated with a rank-1 tensor, $\omega_{i,r}$ is the weight of the rth singular value $\lambda_{i,r}$, each factor vector $\mathbf{u}_{i,r}$ is a unit vector, ρ is a positive constant, and $\tilde{\mathcal{R}}_i$ denotes an operator for grouping similar 2-D patches into a third-order tensor for every exemplar patch $\mathbf{X}_i$. Actually, the proposed intrinsic low-rank tensor approximation can be regarded as a generalization of the matrix nuclear norm minimization to higher order tensors. However, there is still no straightforward algorithm to decompose tensor like the matrix SVD.

B. Tensor Rank-1 Decomposition

Most existing CP algorithms have high computational complexities, such as the CP-ALS [27], [38]. Furthermore, the CP-ALS is hard to obtain a complete set of rank-1 tensors, and thus only works by prescribing the tensor rank. To tackle the above issues, we propose a new tensor rank-1 decomposition algorithm, which is summarized in Algorithm 1. Specifically, for an arbitrary tensor, an initialization procedure is performed

1057-7149 (c) 2018 IEEE. Personal use is permitted, but republication/redistribution requires IEEE permission. See http://www.ieee.org/publications_standards/publications/rights/index.html for more information.

This article has been accepted for publication in a future issue of this journal, but has not been fully edited. Content may change prior to final publication. Citation information: DOI 10.1109/TIP.2018.2889914, IEEE Transactions on Image Processing

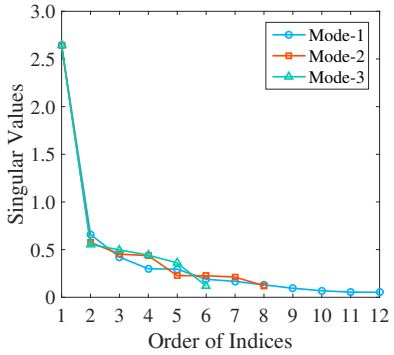

Fig. 2. Singular value curves of three index directions of a random 2×3×4 tensor decomposition.

using the HOSVD [37]. Thus, the tensor is decomposed into a core tensor multiplied by factor matrices along each mode. Next, we gradually select and separate a vector $\mathbf{g}$ that is parallel to a specific mode in the core tensor, and then multiply it by the corresponding factor vectors for composing a rank-1 tensor. For each rank-1 tensor, the factor vectors are normalized to unit vectors, and thus we can obtain the affiliated singular value. Note that, the proposed tensor rank-1 decomposition depends on the direction chosen for the index vector $\mathbf{g}$. In this paper, the direction of the index vector $\mathbf{g}$ is fixed and parallel to patch grouping mode. The main computational cost of our rank-1 decomposition algorithm is from the HOSVD. For example, given an third-order tensor $\mathcal{X} \in \mathbb{R}^{I_1 \times I_2 \times I_3}$, the singular value curves by employing Algorithm 1 are shown in Fig. 2, where the weak bound of the CP-rank satisfies

$$\text{rank}_{\text{CP}}(\mathcal{X} \in \mathbb{R}^{I_1 \times I_2 \times I_3}) \leq \min\{I_1 I_2, I_1 I_3, I_2 I_3\}. \tag{11}$$

Based on the proposed tensor rank-1 decomposition described in Algorithm 1, we can conveniently convert a tensor grouped by similar patches into a finite sum of rank-1 terms,

$$\tilde{\mathcal{R}}_i \mathbf{X} = \sum_r \lambda_{i,r} \mathbf{u}_{i,r}^{(1)} \circ \mathbf{u}_{i,r}^{(2)} \circ \mathbf{u}_{i,r}^{(3)}. \tag{12}$$

Algorithm 1 Proposed Tensor Rank-1 Decomposition

Input: Arbitrary tensor $\mathcal{X} \in \mathbb{R}^{I_1 \times I_2 \times \cdots \times I_N}$
Output: $\mathbf{u}_r^{(n)}$, λ_r, $n = 1, 2, \ldots, N$, $r = 1, 2, 3, \ldots$
  $\mathcal{X} = \mathcal{G} \times_1 \mathbf{U}^{(1)} \times_2 \mathbf{U}^{(2)} \cdots \times_N \mathbf{U}^{(N)} \leftarrow \text{HOSVD}(\mathcal{X})$
  $r = 1$
  while $\mathcal{G} \neq \mathbf{0}$ **do**
    - Choose a nonzero index vector paralleling to mode-m: $\mathbf{g}_r = \mathcal{G}(i_1, \ldots, i_{m-1}, :, i_{m+1}, \ldots, i_N)$
    - $\lambda_r = \|\mathbf{U}^{(m)} \mathbf{g}_r\|_2$
    - $\mathbf{u}_r^{(m)} = \lambda_r^{-1} \mathbf{U}^{(m)} \mathbf{g}_r$
    for $n = 1, \ldots, m-1, m+1, \ldots, N$ **do**
      $\mathbf{u}_r^{(n)} = \mathbf{U}^{(n)}(:, i_n)$
    end
    - $\mathcal{G}(i_1, \ldots, i_{m-1}, :, i_{m+1}, \ldots, i_N) = \mathbf{0}$
    - $r = r + 1$
  end

Specifically, the proposed tensor decomposition algorithm cannot guarantee that it is the optimal rank decomposition, where the rank decomposition represents an exact CP decomposition with $R = \text{rank}(\mathcal{X})$ components.

C. Weighted Intrinsic Low-Rank Tensor Solution

Inspired by the weighted matrix nuclear norm minimization, we weight $\lambda_{i,r}$ in (12) since different singular values may have different effects. The weights and the singular values are both in a descending order. More generally, the soft thresholding and weighting approach is expressed as

$$\widehat{\tilde{\mathcal{R}}_i \mathbf{X}} = \sum_r \omega_{i,r} \lambda_{i,r} \mathbf{u}_{i,r}^{(1)} \circ \mathbf{u}_{i,r}^{(2)} \circ \mathbf{u}_{i,r}^{(3)}, \tag{13}$$

where $\omega_{i,r}$ can take values in [0, 1], where the value 0 masks $\lambda_{i,r}$ truncated. In each iteration, $\lambda_{i,r}$ is assigned with the weight

$$\omega_{i,r} = 2^{-1}(\lambda_{i,r} + (\lambda_{i,r}^2 - c\sqrt{p}\sigma_i^2)^{1/2}), \tag{14}$$

where c is a positive constant, p is the number of grouped patches, σ_i^2 is the noise variance estimated in each iteration. Similarly, the factor vectors along patch grouping mode are also weighted by using (14) to augment patch grouping sparsity. With a back-projection step, we calculate a new noisy observation after obtaining an estimate $\hat{\mathbf{X}}$,

$$\mathbf{Y}' = \hat{\mathbf{X}} + \delta(\mathbf{Y} - \hat{\mathbf{X}}). \tag{15}$$

In particular, we initialize the nonlocal operation using the BM3D estimate [11]. To summarize, the whole denoising algorithm is described in Algorithm 2.

D. Extension to Color Image Denoising

Generally, we extend the proposed WTR1 method to color image denoising. A straightforward implementation strategy of the color version is to apply the grayscale image denoising method to each channel independently. However, such simple operation ignores the spectral correlation among RGB channels. Therefore, instead of computing the patch similarity on

Algorithm 2 Image Denoising by WTR1

Input: Noisy image $\mathbf{Y}$
Output: Denoised image $\hat{\mathbf{X}}$
  Initialization: $\hat{\mathbf{X}}^{(0)} = \mathbf{Y}$, $\mathbf{Y}^{(0)} = \mathbf{Y}$
  while stop criteria unsatisfied **do**
    Noisy observation $\mathbf{Y}^{(k)} = \hat{\mathbf{X}}^{(k-1)} + \delta(\mathbf{Y} - \mathbf{Y}^{(k-1)})$
    for every exemplar patch $\mathbf{X}_i$ in $\mathbf{Y}^{(k)}$ **do**
      - Group similar patches into a 3-D stack $\tilde{\mathcal{R}}_i \mathbf{X}$
      - Compute $\mathbf{u}_r^{(n)}$ and λ_r using the tensor rank-1 decomposition for $\tilde{\mathcal{R}}_i \mathbf{X}$
      - Update σ_i, such that $\sigma_i^2 = \gamma(\sigma^2 - \|\mathbf{Y} - \mathbf{X}\|_F^2)$
      - Estimate weight $\omega_{i,r}$
      - Perform weighted low-rank tensor approximation
    end
    Aggregate the estimated patches $\widehat{\tilde{\mathcal{R}}_i \mathbf{X}}$ to form $\hat{\mathbf{X}}^{(k)}$
  end

1057-7149 (c) 2018 IEEE. Personal use is permitted, but republication/redistribution requires IEEE permission. See http://www.ieee.org/publications_standards/publications/rights/index.html for more information.

This article has been accepted for publication in a future issue of this journal, but has not been fully edited. Content may change prior to final publication. Citation information: DOI 10.1109/TIP.2018.2889914, IEEE Transactions on Image Processing

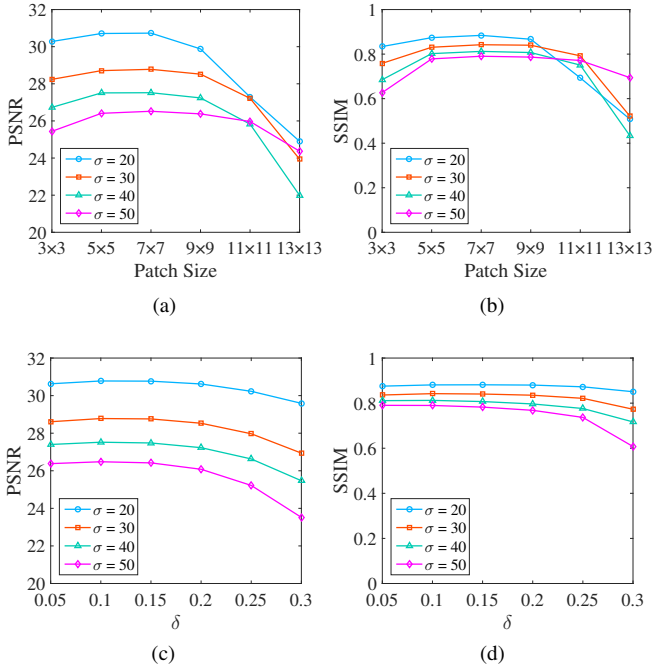

Fig. 3. Influences of the patch size and δ on denoising performance. The testing image is *Cameraman* of size 256×256 with different noise levels. (a) and (b) show the PSNR and SSIM results of different patch sizes, respectively; (c) and (d) show the PSNR and SSIM results of different δ, respectively.

Fig. 4. The testing grayscale images used in the paper.

each channel independently, we first transform color images into a less correlated color space for utilizing the channel correlation, such as YCbCr and opponent color space transformation. Then, the transformed RGB channels are divided into overlapping 3-D patches and the similar 3-D patches are grouped into a 4-D stack. Note that, the grouped 4-D stack of transformed RGB channels is composed by three 3-D stacks. In addition, since three channels may contain different noise statistics, we separately handle each 3-D stack with the way for processing grayscale images.

V. Experimental Results

In this section, experiments on several natural grayscale and color images are conducted to evaluate the performance of the proposed WTR1 method. For fair comparison, all the testing images ([0-255] range) are corrupted by zero-mean Gaussian noise conducted by the MATLAB function *rng* to produce exactly the same noise. For the color version, the noise is added on each channel independently. The quantitative performances of different denoising methods are measured via peak signal-to-noise ratio (PSNR) and structural similarity (SSIM) [39].

A. Grayscale Image Denoising

There are several important parameters involved in the proposed WTR1 method. To analyze the influence of the patch size, we perform our method with different patch sizes and noise levels. As the PSNR and SSIM results shown in Fig. 3(a) and (b), for the higher noise level, the slightly bigger patch size is generally required to capture the varying local geometry. However, a too large patch size would negatively affect sparsity enforcement and also lead to a high computational cost. By experience, combined with the appropriate number of similar patches, the grouped tensor size is finally tuned to 6×6×60, 7×7×80, 7×7×80 and 8×8×110 for noise levels $\sigma = 20, 30, 40, 50$, respectively. Similarly, the influences of the projection parameter δ, varying from 0 to 0.3, are shown in Fig. 3(c) and (d). The parameter δ controls the amount of residual image added to the updated denoised version. As can be seen, the highest PSNR and SSIM are reached when $\delta = 0.1$. Besides, as δ is getting much larger, the denoising performance decreases sharply since more of noisy component remained. The positive c controls the shrinkage operator of low-rank approximation. According to (14), the larger c chose, the more obvious smooth effect will be introduced. It means that more image details would be lost while more noise is removed. Note that, the positive c associated with the singular values mainly effects the local patch geometry, and the positive c associated with the factor vectors along patch grouping mode mainly effects the sparsity enforcement of similar patch grouping. To generate the best denoising performance, c is empirically set to 0.6 and 10.5, respectively. Apart from the patch size, δ and c, γ controls the re-estimation of noise variance. In practice, γ is set to 0.54, 0.56, 0.56 and 0.58 for noise levels $\sigma = 20, 30, 40, 50$, respectively.

We compare the proposed WTR1 method with several state-of-the-art image denoising methods, including BM3D [11], HOSVD [22], NCSR [12], WNNM [21] and LRA-SVD [17]. It should be noted that the HOSVD denoising method is augmented with a Wiener filter step to produce the final result. All the compared denoising methods are tested using the default parameters suggested by the respective authors. We evaluate on 12 widely used grayscale testing images, as also shown in Fig. 4. The PSNR and SSIM results of compared denoising methods are tabulated in Table I, where the highest value is highlighted in bold on each noise level. In most cases, the proposed WTR1 method has higher PSNR and more competitive SSIM than that of the other compared denoising methods. Moreover, both the average PSNR and SSIM of the proposed WTR1 outperform that of other compared methods on all noise levels. For example, for noise level $\sigma = 50$, on average, the proposed WTR1 method is superior to BM3D by 0.49 dB, to HOSVD by 1.25 dB, to NCSR by 0.62 dB, to WNNM by 0.12 dB, and to LRA-SVD by 0.67 dB, respectively.

Table II reports the execution time of the different denoising methods. All experiments performed on a platform of Intel(R)

1057-7149 (c) 2018 IEEE. Personal use is permitted, but republication/redistribution requires IEEE permission. See http://www.ieee.org/publications_standards/publications/rights/index.html for more information.

This article has been accepted for publication in a future issue of this journal, but has not been fully edited. Content may change prior to final publication. Citation information: DOI 10.1109/TIP.2018.2889914, IEEE Transactions on Image Processing

TABLE I
PSNR (dB) / SSIM Comparison of Different Grayscale Image Denoising Methods

	Airplane	*Barbara*	*Boat*	*C. Man*	*Clock*	*Foreman*	*House*	*Lena*	*Monarch*	*Montage*	*Parrot*	*Peppers*	Average
						$\sigma = 20$							
BM3D [11]	32.62	31.18	31.40	30.48	32.67	34.41	33.84	33.03	30.41	33.58	32.21	31.27	32.26
	0.901	0.907	0.888	0.870	0.931	0.902	0.875	0.877	0.919	0.939	0.899	0.889	0.900
HOSVD [22]	32.39	31.42	31.22	30.32	32.26	33.90	33.46	32.80	30.46	32.74	32.07	31.03	32.01
	0.889	0.905	0.881	0.859	0.915	0.884	0.868	0.868	0.907	0.917	0.885	0.876	0.888
NCSR [12]	32.68	31.14	31.29	30.38	32.58	34.36	33.98	32.99	30.66	33.19	32.23	31.19	32.22
	0.904	0.906	0.882	0.869	0.932	0.903	0.877	0.878	0.921	0.941	0.900	0.888	0.900
WNNM [21]	32.91	31.57	31.55	30.71	32.94	34.58	34.11	33.13	31.19	34.15	32.50	31.51	32.57
	0.904	0.912	0.891	0.873	0.933	0.904	0.877	0.879	0.925	0.942	0.900	0.893	0.903
LRA-SVD [17]	32.57	31.68	31.29	30.33	32.41	34.45	33.72	33.20	30.27	32.74	32.42	30.97	32.17
	0.897	0.915	0.884	0.871	0.921	0.900	0.875	0.880	0.914	0.929	0.897	0.884	0.897
WTR1	**32.99**	**31.72**	**31.69**	**30.74**	**33.03**	**34.65**	**34.17**	**33.25**	**31.26**	**34.21**	**32.62**	**31.60**	**32.66**
	0.905	**0.916**	**0.896**	**0.875**	**0.935**	**0.906**	**0.878**	**0.881**	**0.927**	**0.944**	**0.902**	**0.895**	**0.905**
						$\sigma = 30$							
BM3D [11]	30.70	28.98	29.36	28.66	30.56	32.64	32.19	31.23	28.41	31.29	30.18	29.24	30.29
	0.871	0.856	0.843	0.830	0.905	0.876	0.851	0.845	0.883	0.909	0.869	0.851	0.866
HOSVD [22]	30.29	29.10	29.00	28.43	30.02	31.83	31.33	30.81	28.29	30.36	30.01	28.87	29.86
	0.844	0.851	0.825	0.806	0.872	0.841	0.824	0.823	0.862	0.869	0.840	0.827	0.840
NCSR [12]	30.73	28.77	29.17	28.53	30.42	32.53	32.25	31.11	28.52	30.78	30.23	29.06	30.18
	0.878	0.853	0.836	0.829	0.910	0.880	0.855	0.847	0.885	0.915	0.873	0.851	0.868
WNNM [21]	30.97	29.42	29.53	**28.84**	30.77	32.96	32.63	31.44	28.98	31.67	30.58	29.47	30.61
	0.875	0.869	0.848	0.835	0.909	0.881	0.856	0.852	0.892	0.916	0.873	0.859	0.872
LRA-SVD [17]	30.59	29.43	29.19	28.37	30.28	32.72	31.99	31.40	28.21	30.27	30.46	28.96	30.16
	0.858	0.866	0.833	0.813	0.885	0.872	0.842	0.845	0.875	0.892	0.863	0.845	0.857
WTR1	**31.08**	**29.58**	**29.63**	**28.84**	**30.85**	**33.10**	**32.66**	**31.60**	**29.06**	**31.76**	**30.70**	**29.52**	**30.70**
	0.881	**0.875**	**0.852**	**0.836**	**0.914**	**0.886**	**0.858**	**0.857**	**0.896**	**0.923**	**0.878**	**0.862**	**0.877**
						$\sigma = 40$							
BM3D [11]	29.19	27.22	27.80	27.22	28.85	31.20	30.82	29.81	26.76	29.52	28.52	27.74	28.72
	0.842	0.803	0.802	0.799	0.878	0.850	0.829	0.813	0.844	0.879	0.841	0.816	0.833
HOSVD [22]	28.72	27.34	27.40	27.06	28.33	30.20	29.63	29.28	26.71	28.63	28.49	27.29	28.26
	0.799	0.791	0.771	0.756	0.825	0.797	0.779	0.777	0.816	0.819	0.796	0.779	0.792
NCSR [12]	29.31	27.27	27.64	27.08	28.78	31.44	31.05	29.98	26.87	28.81	28.81	27.58	28.72
	0.855	0.800	0.792	0.794	0.890	0.867	0.840	0.827	0.852	0.892	0.853	0.821	0.840
WNNM [21]	29.60	27.73	28.08	27.55	29.23	31.70	31.46	30.09	27.50	29.90	29.21	28.03	29.17
	0.849	0.818	0.810	0.801	0.884	0.860	0.839	0.824	0.860	0.888	0.850	0.827	0.843
LRA-SVD [17]	29.19	27.89	27.75	27.03	28.73	31.38	30.66	30.08	26.70	28.46	29.04	27.54	28.70
	0.826	0.819	0.789	0.772	0.854	0.845	0.816	0.815	0.834	0.855	0.833	0.807	0.822
WTR1	**29.74**	**27.96**	**28.20**	**27.59**	**29.34**	**31.98**	**31.53**	**30.32**	**27.63**	**30.06**	**29.38**	**28.11**	**29.32**
	0.858	**0.829**	**0.815**	**0.807**	**0.893**	**0.871**	**0.845**	**0.833**	**0.867**	**0.900**	**0.859**	**0.832**	**0.851**
						$\sigma = 50$							
BM3D [11]	28.34	26.43	26.85	26.17	27.77	30.32	29.83	29.00	25.76	27.87	27.79	26.60	27.73
	0.828	0.768	0.772	0.777	0.862	0.839	0.817	0.798	0.819	0.858	0.828	0.790	0.813
HOSVD [22]	27.45	26.06	26.14	25.91	26.97	28.84	28.24	28.04	25.47	27.21	27.23	26.09	26.97
	0.754	0.737	0.721	0.709	0.776	0.753	0.734	0.733	0.772	0.767	0.752	0.735	0.745
NCSR [12]	28.23	26.16	26.55	26.07	27.49	30.35	29.92	28.96	25.74	27.52	27.73	26.45	27.60
	0.836	0.759	0.759	0.775	0.869	0.852	0.826	0.807	0.823	0.871	0.835	0.795	0.817
WNNM [21]	28.57	26.80	27.07	26.51	28.04	30.81	30.49	29.24	26.34	28.24	28.18	26.89	28.10
	0.832	0.787	0.782	0.781	0.868	0.849	0.828	0.808	0.836	0.868	0.836	0.801	0.823
LRA-SVD [17]	28.08	26.66	26.59	26.00	27.45	30.27	29.50	28.97	25.60	27.14	27.90	26.48	27.55
	0.790	0.768	0.747	0.736	0.816	0.816	0.785	0.780	0.798	0.822	0.802	0.775	0.786
WTR1	**28.70**	**26.90**	**27.17**	**26.58**	**28.15**	**31.03**	**30.57**	**29.42**	**26.42**	**28.44**	**28.33**	**26.97**	**28.22**
	0.841	**0.793**	**0.786**	**0.787**	**0.878**	**0.858**	**0.833**	**0.817**	**0.840**	**0.879**	**0.844**	**0.806**	**0.830**

TABLE II
EXECUTION TIME (IN MINUTES) COMPARISON ON GRAYSCALE IMAGES OF SIZE 256×256 WITH NOISE LEVEL 25

Methods	BM3D [11]	HOSVD [22]	NCSR [12]	WNNM [21]	LRA-SVD [17]	WTR1
Language	C	C	MATLAB	MATLAB	MATLAB	MATLAB
Execution time	0.01	7.10	2.30	2.56	0.11	5.06

Core(TM) i7-8550U CPU 1.80GHz with 8GB RAM. The main part of the BM3D and the HOSVD are implemented in C, whereas the proposed WTR1 method and other compared methods are implemented in MATLAB. Note that, if the proposed method is coded with C and executed optimally, the running time should be greatly reduced in practice.

The visual comparisons of different denoising methods on noise level $\sigma = 50$ are shown in Figs. 5 and 6. As can be seen, the proposed WTR1 method is also comparable to the state-of-the-art denoising methods. As shown in Fig. 5, our method exhibits good texture preservation. Particularly, compared with the classical tensor approach HOSVD, the HOSVD denoising

1057-7149 (c) 2018 IEEE. Personal use is permitted, but republication/redistribution requires IEEE permission. See http://www.ieee.org/publications_standards/publications/rights/index.html for more information.

This article has been accepted for publication in a future issue of this journal, but has not been fully edited. Content may change prior to final publication. Citation information: DOI 10.1109/TIP.2018.2889914, IEEE Transactions on Image Processing

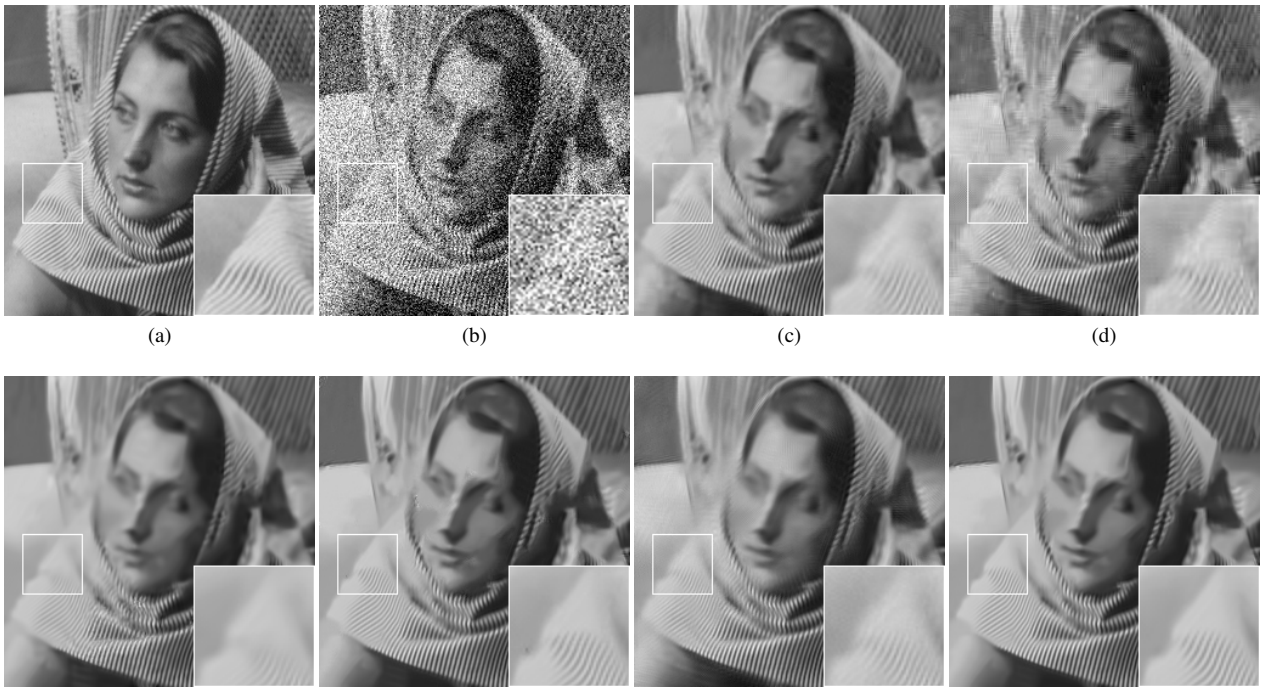

(a) (b) (c) (d)

(e) (f) (g) (h)

Fig. 5. Denoising results of the grayscale image *Barbara*. (a) Ground truth; (b) Noisy image ($\sigma = 50$); (c) BM3D [11] (PSNR = 26.43 dB); (d) HOSVD [22] (PSNR = 26.06 dB); (e) NCSR [12] (PSNR = 26.16 dB); (f) WNNM [21] (PSNR = 26.80 dB); (g) LRA-SVD [17] (PSNR = 26.66 dB); (h) WTR1 (PSNR = **26.90** dB).

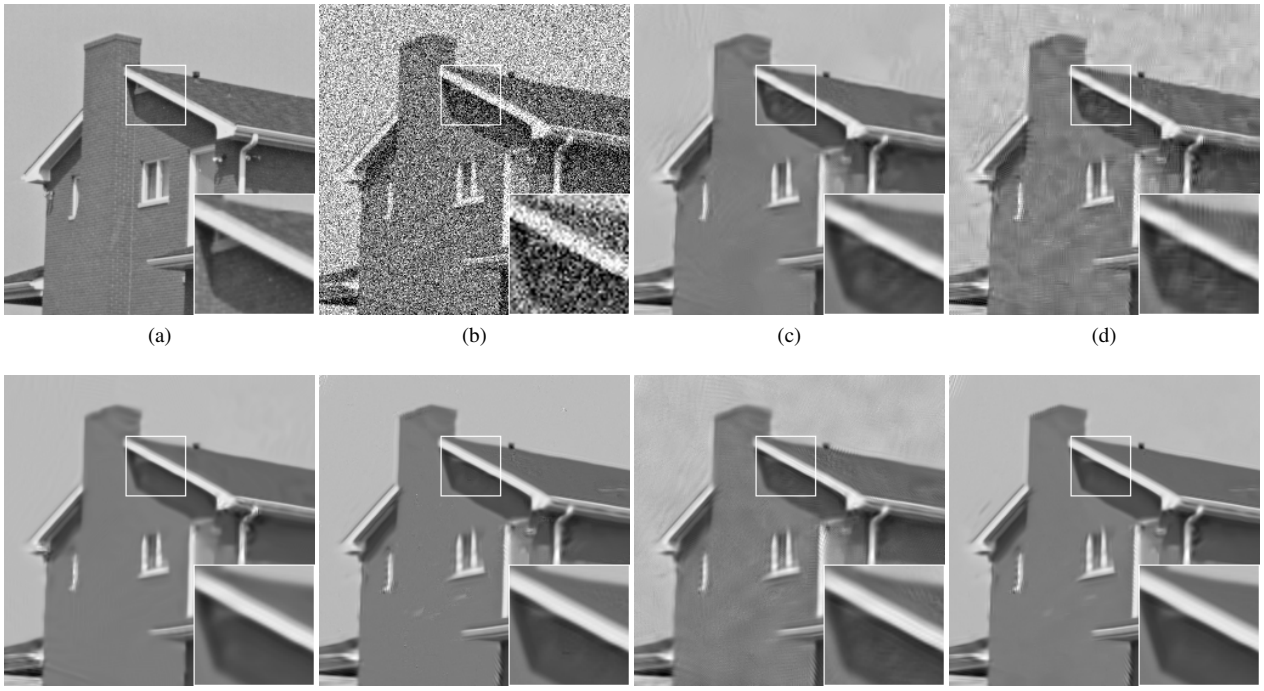

(a) (b) (c) (d)

(e) (f) (g) (h)

Fig. 6. Denoising results of the grayscale image *House*. (a) Ground truth; (b) Noisy image ($\sigma = 50$); (c) BM3D [11] (PSNR = 29.83 dB); (d) HOSVD [22] (PSNR = 28.24 dB); (e) NCSR [12] (PSNR = 29.92 dB); (f) WNNM [21] (PSNR = 30.49 dB); (g) LRA-SVD [17] (PSNR = 29.50 dB); (h) WTR1 (PSNR = **30.57** dB).

method based on the factor matrix truncation strategy would loss more information and generate obvious artifacts. In addition, we also observe that the performance of the WNNM method is close to that of the proposed WTR1. This is because that the local patch geometry is insensitive compared with the similar patch grouping for sparsity enforcement. As shown

1057-7149 (c) 2018 IEEE. Personal use is permitted, but republication/redistribution requires IEEE permission. See http://www.ieee.org/publications_standards/publications/rights/index.html for more information.

This article has been accepted for publication in a future issue of this journal, but has not been fully edited. Content may change prior to final publication. Citation information: DOI 10.1109/TIP.2018.2889914, IEEE Transactions on Image Processing

Fig. 7. The testing color images used in the paper.

TABLE III
PSNR (dB) / MSSIM Comparison of Different Color Image Denoising Methods

	Airplane	*Barbara*	*Boats*	*Butterfly*	*Couple*	*Fence*	*House*	*Lena*	*Tower*	*Voit*	Average
$\sigma_R = \sigma_G = \sigma_B = 30$											
BM3D [11]	31.93	30.64	29.38	29.10	31.41	29.98	29.49	31.58	32.27	27.87	30.37
	0.884	0.875	0.845	0.915	0.825	0.879	0.859	0.824	0.869	0.755	0.853
4D-HOSVD [22]	32.08	30.99	29.41	29.40	31.51	30.09	29.68	31.43	32.29	27.75	30.46
	0.882	0.881	0.841	0.916	0.831	0.869	0.857	0.817	0.865	0.735	0.849
PID [40]	32.29	30.94	29.55	29.38	31.55	30.21	29.65	31.82	32.57	27.92	30.59
	0.888	0.885	0.849	0.922	0.825	0.882	0.859	0.827	0.874	0.757	0.857
WTR1	**32.39**	**31.21**	**29.75**	**30.29**	**31.64**	**30.67**	**29.86**	**31.83**	**32.72**	**28.31**	**30.87**
	0.890	**0.890**	**0.856**	**0.928**	**0.834**	**0.888**	**0.865**	**0.828**	**0.875**	**0.774**	**0.863**
$\sigma_R = \sigma_G = \sigma_B = 40$											
BM3D [11]	30.26	28.81	27.77	27.14	29.80	28.14	27.93	30.08	30.54	26.38	28.69
	0.853	0.827	0.792	0.878	0.763	0.832	0.812	0.791	0.831	0.687	0.807
4D-HOSVD [22]	30.77	29.49	28.03	27.90	30.23	28.76	28.33	30.34	30.86	26.63	29.13
	0.860	0.845	0.800	0.892	0.792	0.835	0.821	0.794	0.835	0.686	0.816
PID [40]	31.09	29.56	28.21	28.11	30.30	28.94	28.36	30.82	31.27	26.68	29.33
	0.870	0.852	0.804	0.904	0.785	0.846	0.825	0.809	0.848	0.692	0.824
WTR1	**31.21**	**29.70**	**28.41**	**28.85**	**30.41**	**29.34**	**28.59**	**30.86**	**31.42**	**27.11**	**29.59**
	0.873	**0.854**	**0.815**	**0.911**	**0.796**	**0.855**	**0.834**	**0.810**	**0.852**	**0.720**	**0.832**
$\sigma_R = \sigma_G = \sigma_B = 50$											
BM3D [11]	29.84	28.36	27.05	26.57	29.23	27.85	27.37	29.85	29.91	25.73	28.18
	0.850	0.817	0.768	0.870	0.753	0.820	0.798	0.789	0.821	0.654	0.794
4D-HOSVD [22]	29.72	28.35	27.01	26.74	29.21	27.77	27.30	29.42	29.79	25.81	28.11
	0.839	0.814	0.765	0.869	0.758	0.807	0.788	0.772	0.809	0.651	0.787
PID [40]	30.11	28.50	27.18	27.12	29.29	28.00	27.35	30.00	30.24	25.76	28.36
	0.854	0.823	0.766	0.886	0.749	0.818	0.794	0.793	0.825	0.644	0.795
WTR1	**30.29**	**28.59**	**27.41**	**27.74**	**29.48**	**28.40**	**27.64**	**30.07**	**30.39**	**26.23**	**28.62**
	0.858	**0.824**	**0.780**	**0.894**	**0.761**	**0.830**	**0.807**	**0.794**	**0.830**	**0.677**	**0.806**
$\sigma_R = 40, \sigma_G = 30, \sigma_B = 50$											
BM3D [11]	30.55	29.08	27.81	27.43	29.93	28.56	28.11	30.45	30.67	26.43	28.90
	0.854	0.832	0.790	0.880	0.773	0.837	0.817	0.796	0.828	0.684	0.809
4D-HOSVD [22]	30.48	29.03	27.79	27.63	29.84	28.52	28.02	30.10	30.56	26.38	28.84
	0.853	0.833	0.791	0.885	0.773	0.828	0.812	0.789	0.829	0.677	0.807
PID [40]	30.79	29.20	27.92	27.69	30.06	28.61	28.04	30.61	31.02	26.44	29.04
	0.863	0.843	0.795	0.894	0.776	0.840	0.817	0.805	0.842	0.684	0.816
WTR1	**31.09**	**29.57**	**28.30**	**28.74**	**30.32**	**29.22**	**28.44**	**30.78**	**31.30**	**27.00**	**29.48**
	0.870	**0.851**	**0.812**	**0.910**	**0.794**	**0.852**	**0.830**	**0.808**	**0.850**	**0.715**	**0.829**

in Fig. 6, our method outputs smoother surfaces in the homogeneous regions compared with the WNNM. The superior performance of the proposed WTR1 method demonstrates the effectiveness of exploiting the local patch geometry.

B. Color Image Denoising

We also compare the denoising performance of the proposed WTR1 method with the CBM3D [11], 4D-HOSVD [22] and progressive image denoising (PID) [40] for the color version. In our experiments, we use 10 widely used color images as testing images, as also shown in Fig. 7. Specifically, for the RGB channels characterized by different noise statistics, we set the average noise deviation for the methods which support only a single noise level parameter input:

$$\sigma = (3^{-1}(\sigma_R^2 + \sigma_G^2 + \sigma_B^2))^{1/2}. \tag{16}$$

The results with different noise levels and distributions are presented in Table III. Note that, the mean SSIM (MSSIM) index is calculated by

$$\text{MSSIM} = 3^{-1} \sum_{c=R,G,B} \text{SSIM}(\mathbf{X}_c, \hat{\mathbf{X}}_c). \tag{17}$$

Numerically, it can be seen that our results are clearly better than that of the other compared denoising methods. The visual comparisons are inspected in Figs. 8 and 9. As can be observed, the proposed WTR1 method can better restore the detailed information, like fine lines in Fig. 8. Specifically, for the visual performance of the flat regions in Fig. 9, the proposed WTR1 method is intuitively competitive compared with the other methods. Meanwhile, our method can produce sharper transitions, like the zoomed region in Fig. 9.

1057-7149 (c) 2018 IEEE. Personal use is permitted, but republication/redistribution requires IEEE permission. See http://www.ieee.org/publications_standards/publications/rights/index.html for more information.

This article has been accepted for publication in a future issue of this journal, but has not been fully edited. Content may change prior to final publication. Citation information: DOI 10.1109/TIP.2018.2889914, IEEE Transactions on Image Processing

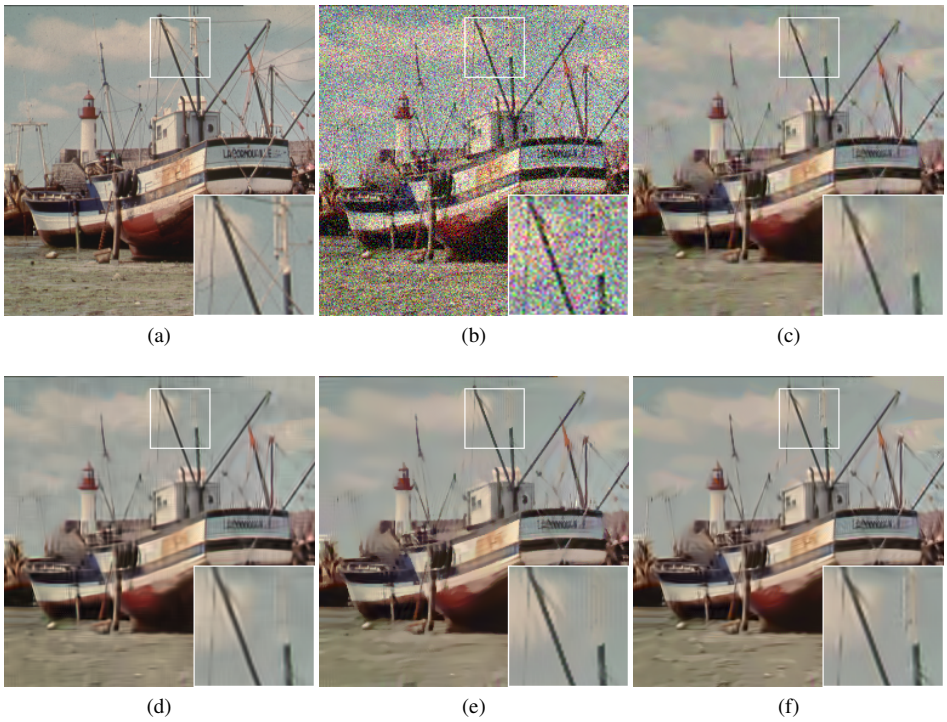

(a) (b) (c)

(d) (e) (f)

Fig. 8. Denoising results of the color image *Boats*. (a) Ground truth; (b) Noisy image ($\sigma_R = \sigma_G = \sigma_B = 40$); (c) CBM3D [11] (PSNR = 27.77 dB); (d) 4D-HOSVD [22] (PSNR = 28.03 dB); (e) PID [40] (PSNR = 28.21 dB); (f) WTR1 (PSNR = **28.41** dB).

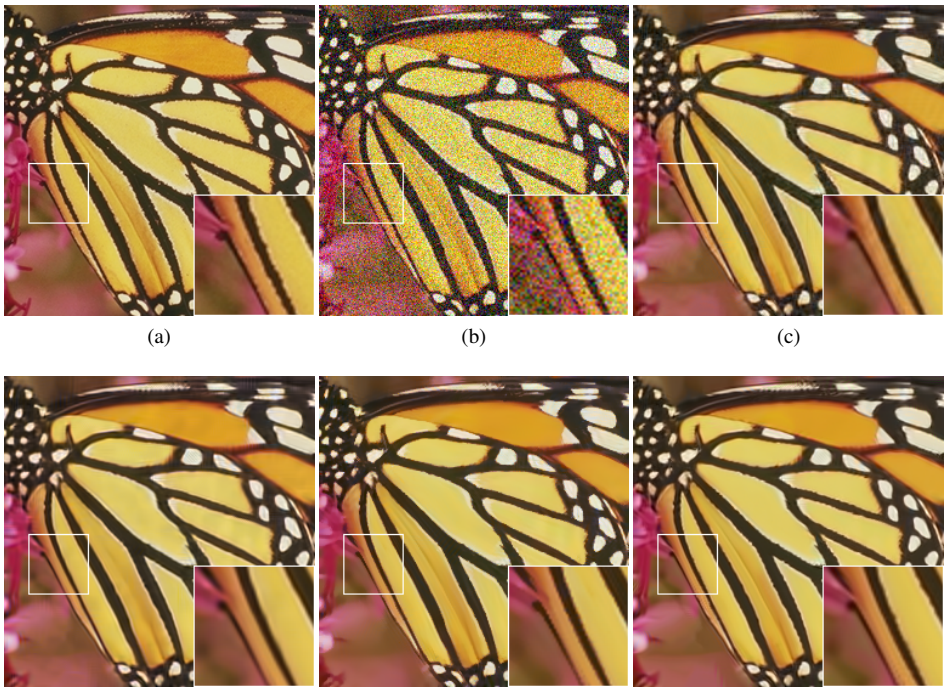

(a) (b) (c)

(d) (e) (f)

Fig. 9. Denoising results of the color image *Butterfly*. (a) Ground truth; (b) Noisy image ($\sigma_R = 40, \sigma_G = 30, \sigma_B = 50$); (c) CBM3D [11] (PSNR = 27.43 dB); (d) 4D-HOSVD [22] (PSNR = 27.63 dB); (e) PID [40] (PSNR = 27.69 dB); (f) WTR1 (PSNR = **28.74** dB).

C. Real-World Image Denoising

We have tested the proposed method on two real-world noisy image datasets. The Dataset 1 is the RENOIR [41]. The acquisition procedure of the RENOIR dataset is carried out by taking sets of static scenes with different light sensitivity (ISO) values, and the low-ISO images are served as references. Since the image size in the RENOIR dataset is very large, we have randomly cropped 120 smaller images of size 512×512

1057-7149 (c) 2018 IEEE. Personal use is permitted, but republication/redistribution requires IEEE permission. See http://www.ieee.org/publications_standards/publications/rights/index.html for more information.

This article has been accepted for publication in a future issue of this journal, but has not been fully edited. Content may change prior to final publication. Citation information: DOI 10.1109/TIP.2018.2889914, IEEE Transactions on Image Processing

Fig. 10. Some sample images from the Dataset 1.

Fig. 11. Some sample images from the Dataset 2.

TABLE IV
MEAN PSNR (dB) / MSSIM Comparison of Different Color Image Denoising Methods Tested on Different Datasets

	Dataset 1	Dataset 2
BM3D [11]	30.14 0.775	35.98 0.920
4D-HOSVD [22]	29.55 0.753	35.70 0.914
PID [40]	29.91 0.782	36.03 0.924
WTR1	**30.99** **0.810**	**36.73** **0.936**

for experiments. Some samples are shown in Fig. 10. The Dataset 2 contains 17 images which were captured from 11 static scenes [42]. Each scene in the Dataset 2 was shot 500 times and the mean image is taken as reference. Similar to the Dataset 1, 50 smaller images of size 512×512 have been randomly cropped for experiments. Some samples are shown in Fig. 11. The experimental results on the two datasets are presented in Table IV. As can be seen, the proposed WTR1 method consistently outperforms the other compared methods. Figs. 12 and 13 show the visual comparisons of different denoising methods. Intuitively, compared with the other methods, the proposed WTR1 method can better preserve image details. In addition, our method can obviously reduce more noise level, especially at the zoomed region in Fig. 12.

VI. CONCLUSIONS

This paper presents a novel weighted tensor rank-1 decomposition method for nonlocal image denoising. To effectively exploit the local and nonlocal self-similarity jointly for low-rank models, we preserve the matrix form of each patch and convert it to tensor problem. By developing a new efficient tensor rank-1 decomposition algorithm, we can conveniently decompose an arbitrary tensor into a finite sum of rank-1 products and manipulate the CP-rank. The proposed WTR1 method provides a feasible intrinsic low-rank tensor approximation strategy which has remained elusive to the best of our knowledge. Experimental results have demonstrated that the proposed WTR1 method performs better than several state-of-the-art denoising methods.

In our future works, we will apply the proposed WTR1 method to other modalities of image data, such as videos, hyperspectral images, MRI images, etc. Besides, the proposed technique is a general and effective tool to capture the nonlocal information in the data which is of low-rank. Therefore, it is applicable to more other inverse problems, such as inpainting, super-resolution and compressive sensing.

ACKNOWLEDGMENT

The authors would like to thank the editors and anonymous reviewers for their insightful comments and suggestions, which have greatly improved this paper.

REFERENCES

[1] A. Beck and M. Teboulle, "Fast gradient-based algorithms for constrained total variation image denoising and deblurring problems," *IEEE Trans. Image Process.*, vol. 18, no. 11, pp. 2419-2434, Nov. 2009.
[2] G. R. Easley, D. Labate, and F. Colonna, "Shearlet-based total variation diffusion for denoising," *IEEE Trans. Image Process.*, vol. 18, no. 2, pp. 260-268, Feb. 2009.
[3] M. Elad and M. Aharon, "Image denoising via sparse and redundant representations over learned dictionaries," *IEEE Trans. Image Process.*, vol. 15, no. 12, pp. 3736-3745, Dec. 2006.
[4] M. Protter and M. Elad, "Image sequence denoising via sparse and redundant representations," *IEEE Trans. Image Process.*, vol. 18, no. 1, pp. 27-35, Jan. 2009.
[5] J. Yang, Z. Gan, Z. Wu, and C. Hou, "Estimation of signal-dependent noise level function in transform domain via a sparse recovery model," *IEEE Trans. Image Process.*, vol. 24, no. 5, pp. 1561-1572, May 2015.
[6] L. Fang, S. Li, D. Cunefare, and S. Farsiu, "Segmentation based sparse reconstruction of optical coherence tomography images," *IEEE Trans. Med. Imag.*, vol. 36, no. 2, pp. 407-421, Feb. 2017.
[7] U. Schmidt and S. Roth, "Shrinkage fields for effective image restoration," in *Proc. IEEE Conf. Comput. Vis. Pattern Recognit.*, 2014, pp. 2774-2781.
[8] Y. Chen, Wei Yu, and T. Pock, "On learning optimized reaction diffusion processes for effective image restoration," in *Proc. IEEE Conf. Comput. Vis. Pattern Recognit.*, 2015, pp. 5261-5269.
[9] K. Zhang, W. Zuo, Y. Chen, D. Meng, and L. Zhang, "Beyond a Gaussian denoiser: Residual learning of deep CNN for image denoising," *IEEE Trans. Image Process.*, vol. 26, no. 7, pp. 3142-3155, Jul. 2017.
[10] A. Buades, B. Coll, and J.-M. Morel, "A non-local algorithm for image denoising," in *Proc. IEEE Conf. Comput. Vis. Pattern Recognit.*, 2005, pp. 60-65.
[11] K. Dabov, A. Foi, V. Katkovnik, and K. Egiazarian, "Image denoising by sparse 3-D transform-domain collaborative filtering," *IEEE Trans. Image Process.*, vol. 16, no. 8, pp. 2080-2095, Aug. 2007.
[12] W. Dong, L. Zhang, G. Shi, and X. Li, "Nonlocally centralized sparse representation for image restoration," *IEEE Trans. Image Process.*, vol. 22, no. 4, pp. 1620-1630, Apr. 2013.
[13] M. Lebrun, A. Buades, and J. M. Morel, "A nonlocal Bayesian image denoising algorithm," *SIAM J. Imag. Sci.*, vol. 6, no. 3, pp. 1665-1688, Sep. 2013.
[14] H. Liu, R. Xiong, J. Zhang, and W. Gao, "Image denoising via adaptive soft-thresholding based on non-local samples," in *Proc. IEEE Conf. Comput. Vis. Pattern Recognit.*, 2015, pp. 484-492.
[15] R. Wang and D. Tao, "Non-local auto-encoder with collaborative stabilization for image restoration," *IEEE Trans. Image Process.*, vol. 25, no. 5, pp. 2117-2129, May 2016.
[16] J. Pang and G. Cheung, "Graph Laplacian regularization for image denoising: Analysis in the continuous domain," *IEEE Trans. Image Process.*, vol. 26, no. 4, pp. 1770-1785, Apr. 2017.
[17] Q. Guo, C. Zhang, Y. Zhang, and H. Liu, "An efficient SVD-based method for image denoising," *IEEE Trans. Circuits Syst. Video Technol.*, vol. 26, no. 5, pp. 868-880, May 2016.
[18] M. Fazel, H. Hindi, and S. P. Boyd, "A rank minimization heuristic with application to minimum order system approximation," in *Proc. Am. Control Conf.*, 2001, pp. 4734-4739.

1057-7149 (c) 2018 IEEE. Personal use is permitted, but republication/redistribution requires IEEE permission. See http://www.ieee.org/publications_standards/publications/rights/index.html for more information.

This article has been accepted for publication in a future issue of this journal, but has not been fully edited. Content may change prior to final publication. Citation information: DOI 10.1109/TIP.2018.2889914, IEEE Transactions on Image Processing

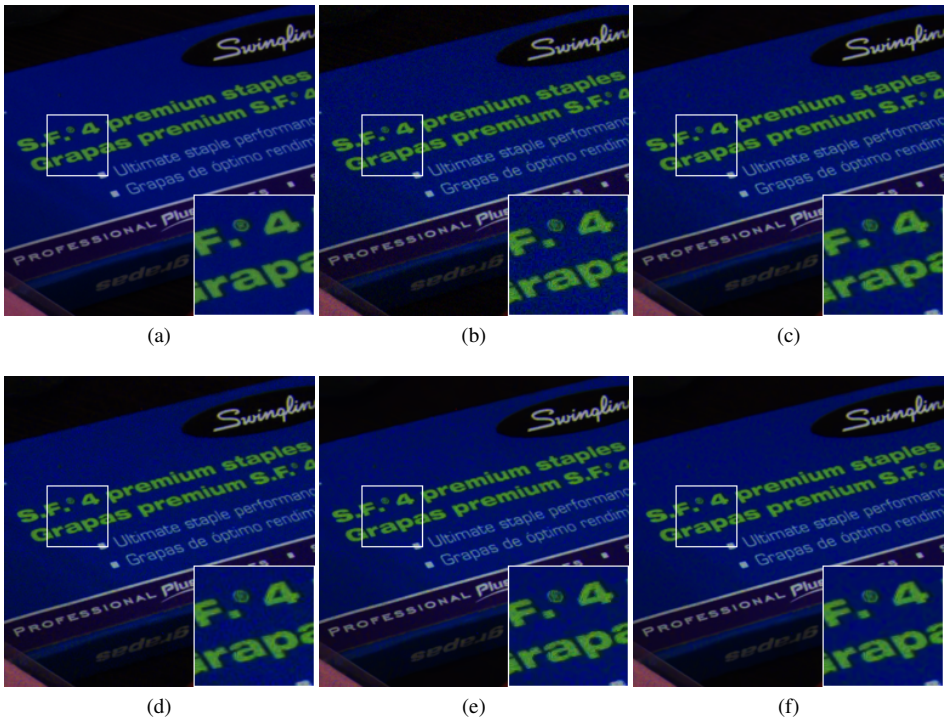

(a) (b) (c)

(d) (e) (f)

Fig. 12. Denoising results of a real-world image from the Dataset 1. (a) Reference; (b) Noisy image; (c) CBM3D [11] (PSNR = 32.15 dB); (d) 4D-HOSVD [22] (PSNR = 31.46 dB); (e) PID [40] (PSNR = 31.73 dB); (f) WTR1 (PSNR = **33.10** dB).

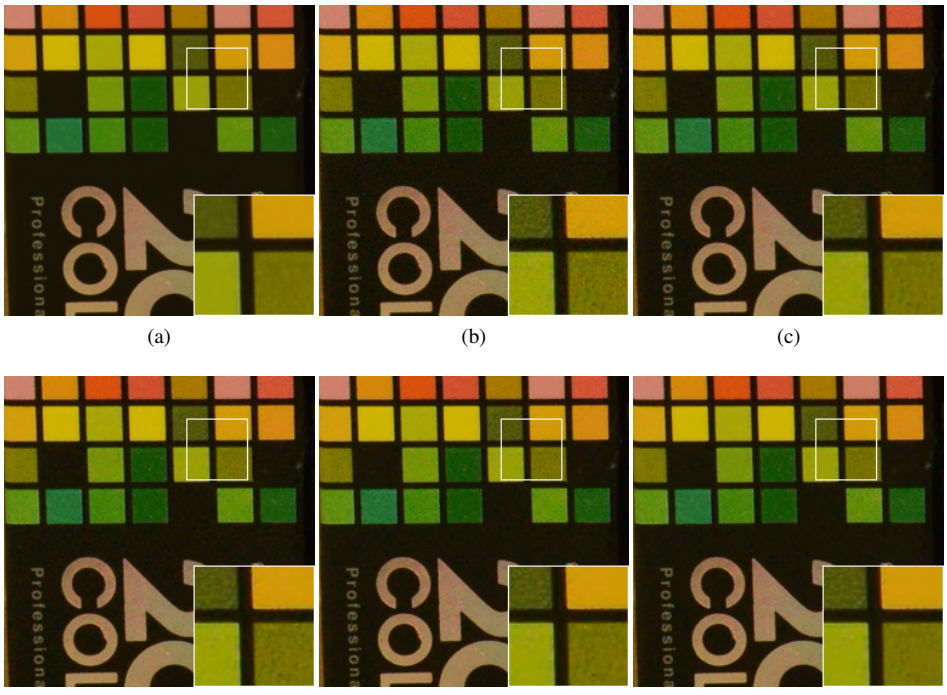

(a) (b) (c)

(d) (e) (f)

Fig. 13. Denoising results of a real-world image from the Dataset 2. (a) Reference; (b) Noisy image; (c) CBM3D [11] (PSNR = 35.38 dB); (d) 4D-HOSVD [22] (PSNR = 35.01 dB); (e) PID [40] (PSNR = 35.40 dB); (f) WTR1 (PSNR = **36.27** dB).

[19] J.-F. Cai, E. J. Candès, and Z. Shen. "A singular value thresholding algorithm for matrix completion," *SIAM J. Optim.*, vol. 20, no. 4, pp. 1956-1982, Mar. 2010.

[20] W. Dong, G. Shi, and X. Li, "Nonlocal image restoration with bilateral variance estimation: A low-rank approach," *IEEE Trans. Image Process.*, vol. 22, no. 2, pp. 700-711, Feb. 2013.

[21] S. Gu, L. Zhang, W. Zuo, and X. Feng, "Weighted nuclear norm minimization with application to image denoising," in *Proc. IEEE Conf. Comput. Vis. Pattern Recognit.*, 2014, pp. 2862-2869.

[22] A. Rajwade, A. Rangarajan, and A. Banerjee, "Image denoising using the higher order singular value decomposition," *IEEE Trans. Pattern Anal. Mach. Intell.*, vol. 35, no. 4, pp. 849-862, Apr. 2013.

1057-7149 (c) 2018 IEEE. Personal use is permitted, but republication/redistribution requires IEEE permission. See http://www.ieee.org/publications_standards/publications/rights/index.html for more information.

This article has been accepted for publication in a future issue of this journal, but has not been fully edited. Content may change prior to final publication. Citation information: DOI 10.1109/TIP.2018.2889914, IEEE Transactions on Image Processing

[23] B. Du, M. Zhang, L. Zhang, R. Hu, and D. Tao, "PLTD: Patch-based low-Rank tensor decomposition for hyperspectral images," *IEEE Trans. Multimedia*, vol. 19, no. 1, pp. 67-79, Jan. 2017.
[24] M. Rezghi, "A novel fast tensor-based preconditioner for image restoration," *IEEE Trans. Image Process.*, vol. 26, no. 9, pp. 4499-4508, Sep. 2017.
[25] J. Liu, P. Musialski, P. Wonka, and J. Ye, "Tensor completion for estimating missing values in visual data," *IEEE Trans. Pattern Anal. Mach. Intell.*, vol. 35, no. 1, pp. 208-220, Jan. 2013.
[26] Q. Zhao, D. Meng, X. Kong, Q. Xie, W. Cao, Y. Wang, and Z. Xu, "A novel sparsity measure for tensor recovery," in *Proc. IEEE Int. Conf. Comput. Vis.*, 2015, pp. 271-279.
[27] J. D. Carroll and J.-J. Chang, "Analysis of individual differences in multidimensional scaling via an n-way generalization of "Eckart-Young" decomposition," *Psychometrika*, vol. 35, no. 3, pp. 283-319, Sep. 1970.
[28] H. Takeda, S. Farsiu, and P. Milanfar, "Kernel regression for image processing and reconstruction," *IEEE Trans. Image Process.*, vol. 16, no. 2, pp. 349-366, Feb. 2007.
[29] V. Katkovnik, A. Foi, K. Egiazarian, and J. Astola, "From local kernel to nonlocal multiple-model image denoising," *Int. J. Comput. Vis.*, vol. 86, no. 1, pp. 1-32, Jan. 2010.
[30] L. Shao, R. Yan, X. Li, and Y. Liu, "From heuristic optimization to dictionary learning: A review and comprehensive comparison of image denoising algorithms," *IEEE Trans. Cybern.*, vol. 44, no. 7, pp. 1001-1013, Jul. 2014.
[31] N. Srebro and T. Jaakkola, "Weighted low-rank approximations," in *Proc. Int. Conf. Mach. Learn.*, 2003, pp. 720-727.
[32] A. M. Buchanan and A. W. Fitzgibbon, "Damped Newton algorithms for matrix factorization with missing data," in *Proc. IEEE Conf. Comput. Vis. Pattern Recognit.*, 2005, pp. 316-322.
[33] Q. Ke and T. Kanade, "Robust l_1 norm factorization in the presence of outliers and missing data by alternative convex programming," in *Proc. IEEE Conf. Comput. Vis. Pattern Recognit.*, 2005, pp. 739-746.
[34] A. Eriksson and A. van den Hengel, "Efficient computation of robust low-rank matrix approximations in the presence of missing data using the l_1 norm," in *Proc. IEEE Conf. Comput. Vis. Pattern Recognit.*, 2010, pp. 771-778.
[35] B. Recht, M. Fazel, and P. A. Parrilo, "Guaranteed minimum-rank solutions of linear matrix equations via nuclear norm minimization," *SIAM Rev.*, vol. 52, no. 3, pp. 471-501, Aug. 2010.
[36] L. R. Tucker, "Some mathematical notes on three-mode factor analysis," *Psychometrika*, vol. 31, no. 3, pp. 279-311, Sep. 1966.
[37] L. De Lathauwer, B. De Moor, and J. Vanderwalle, "A multilinear singular value decomposition," *SIAM J. Matrix Anal. Appl.*, vol. 21, no. 4, pp. 1253-1278, Apr. 2000.
[38] T. G. Kolda and B. W. Bader, "Tensor decompositions and applications," *SIAM Rev.*, vol. 51, no. 3, pp. 455-500, Aug. 2009.
[39] Z. Wang, A. C. Bovik, H. R. Sheikh, and E. P. Simoncelli, "Image quality assessment: From error visibility to structural similarity," *IEEE Trans. Image Process.*, vol. 13, no. 4, pp. 600-612, Apr. 2004.
[40] C. Knaus and M. Zwicker, "Progressive image denoising," *IEEE Trans. Image Process.*, vol. 23, no. 7, pp. 3114-3125, Jul. 2014.
[41] J. Anaya and A. Barbu, "RENOIR - A dataset for real low-light image noise reduction," *J. Vis. Commun. Image Represent.*, vol. 51, pp. 144-154, Feb. 2018.
[42] S. Nam, Y. Hwang, Y. Matsushita, and S. J. Kim, "A holistic approach to cross-channel image noise modeling and its application to image denoising," in *Proc. IEEE Conf. Comput. Vis. Pattern Recognit.*, 2016, pp. 1683-1691.

Yue Wu (S'17) received the B.E. degree from the College of Electrical and Information Engineering, Hunan University, Changsha, China, in 2015. He is currently pursuing the Ph.D. degree with the College of Electrical and Information Engineering, Hunan University, Changsha, China. His research interests include image processing, remote sensing and compressive sensing.

Leyuan Fang (S'10-M'14-SM'17) received the Ph.D. degree from the College of Electrical and Information Engineering, Hunan University, Changsha, China, in 2015.

From September 2011 to September 2012, he was a visiting Ph.D. student with the Department of Ophthalmology, Duke University, Durham, NC, USA, supported by the China Scholarship Council. From August 2016 to September 2017, he was a Postdoctoral Research Fellow with the Department of Biomedical Engineering, Duke University, Durham, NC, USA. Since January 2017, he has been an associate professor with the College of Electrical and Information Engineering, Hunan University. His research interests include sparse representation and multi-resolution analysis in remote sensing and medical image processing. He has won the Scholarship Award for Excellent Doctoral Student granted by Chinese Ministry of Education in 2011.

Shutao Li (M'07-SM'15-F'19) received the B.S., M.S., and Ph.D. degrees from Hunan University, Changsha, China, in 1995, 1997, and 2001, respectively. He was a Research Associate with the Department of Computer Science, the Hong Kong University of Science and Technology, Hong Kong, in 2011. From 2002 to 2003, he was a Post-Doctoral Fellow with the Royal Holloway College, University of London, London, U.K., with Prof. John Shawe-Taylor. In 2005, he visited the Department of Computer Science, Hong Kong University of Science and Technology as a Visiting Professor. He joined the College of Electrical and Information Engineering, Hunan University, in 2001. He is currently a Full Professor with the College of Electrical and Information Engineering, Hunan University. He has authored or co-authored over 160 refereed papers. His current research interests include image processing, pattern recognition, and artificial intelligence.

He is now an Associate Editor of the IEEE TRANSACTIONS ON GEOSCIENCE AND REMOTE SENSING, IEEE TRANSACTIONS ON INSTRUMENTATION AND MEASUREMENT, and a member of the Editorial Board of the Information Fusion and the Sensing and Imaging. He was a recipient of two 2nd-Grade National Awards at the Science and Technology Progress of China in 2004 and 2006.

1057-7149 (c) 2018 IEEE. Personal use is permitted, but republication/redistribution requires IEEE permission. See http://www.ieee.org/publications_standards/publications/rights/index.html for more information.